International Journal of Nanomedicine

Dovepress
Taylor & Francis Group

Open Access Full Text Article

ORIGINAL RESEARCH

Polydopamine Dual-Modal Nanotherapy Synergizes Photothermal Antibacterial and Nanozyme Anti-Inflammatory Effects for Periodontitis Treatment

Jun Guo[1–3], Yifan Liu[1–3], Yi Zhang[1–3], Yuyao Li[1–3], Yunlong Li[1–3], Jian Yang[1–3]

[1]School of Stomatology, Jiangxi Medical College, Nanchang University, Nanchang, 330006, People's Republic of China; [2]Jiangxi Provincial Key Laboratory of Oral Diseases, Nanchang, 330006, People's Republic of China; [3]Jiangxi Provincial Clinical Research Center for Oral Diseases, Nanchang, 330006, People's Republic of China

Correspondence: Jian Yang, Email jianyang@ncu.edu.cn

Introduction: Given the limitations associated with clinical curettage in the treatment of periodontitis, there is a pressing need to enhance the complete removal of plaque from deep periodontal pockets and to facilitate the repair of periodontal tissues through appropriate medical interventions. Despite the significant advancements of various local drug delivery systems (LDDS) for the adjunctive treatment of periodontitis, their efficacy remains constrained by two intertwined challenges: inadequate antibiofilm capability and excessive reactive oxygen species (ROS)-mediated tissue damage.

Methods: To simultaneously overcome these dual barriers, we synthesized polydopamine nanoparticles (PDA NPs) through a straightforward and efficient self-polymerization process of dopamine, followed by the synthesis of nanoparticles on the surface via reductive methods to create multifunctional nanoplatforms (PAg).

Results: Notably, these PDA nanoparticles, which are based on comprehensive nanocomposites, function as photothermal agents that enhance the therapeutic efficacy against biofilms in vitro through antibacterial photothermal therapy (PTT) under near-infrared laser irradiation. Furthermore, owing to the enzyme-like activity of PDA nanozyme, the engineered nanocomposite is capable of effectively scavenging ROS in Raw267.4 cells and human periodontal ligament cells under oxidative stress conditions. The in vitro and in vivo analyses demonstrated that live/dead staining of the biofilm, along with Western blot assessments of inflammatory markers, substantially augmented the antibacterial and anti-inflammatory efficacy. The nano-platform-based PAg nanoparticles developed in our study not only markedly enhanced the antibacterial effect through combination therapy but also efficiently reduced cellular ROS via the enzyme-like activity of the nanozyme.

Conclusion: This dual-modal nanotherapy delivers a coordinated attack on periodontitis pathogenesis, including direct physical elimination of biofilms coupled with ROS scavenging to mitigate collateral tissue damage, thereby addressing the limitations of current LDDS.

Keywords: periodontitis, mild photothermal therapy, ROS, antibacterial, anti-inflammation

Introduction

The primary pathogenic mechanism of chronic periodontitis is attributed to the imbalance between the host immune response and pathogenic bacteria from the dental plaque.[1–3] The harmful products released by bacteria induce the activation of immune cells, generating excessive reactive oxygen species (ROS), upregulating the expression of pro-inflammatory cytokines, and promoting the degradation of periodontal fibers and alveolar bone, thereby causing severe damage to periodontal tissues.[4–7] New treatment strategies for periodontitis pay more attention to the occurrence and development mechanisms of the disease to achieve targeted treatment and obtain highly efficient therapeutic effects.[8,9] According to the occurrence and development mechanisms of periodontitis, if the periodontal microenvironment can be reshaped, the imbalance between the immune response and pathogenic bacteria can be effectively regulated, significantly

Received: 9 June 2025
Accepted: 2 September 2025
Published: 20 September 2025

Graphical Abstract

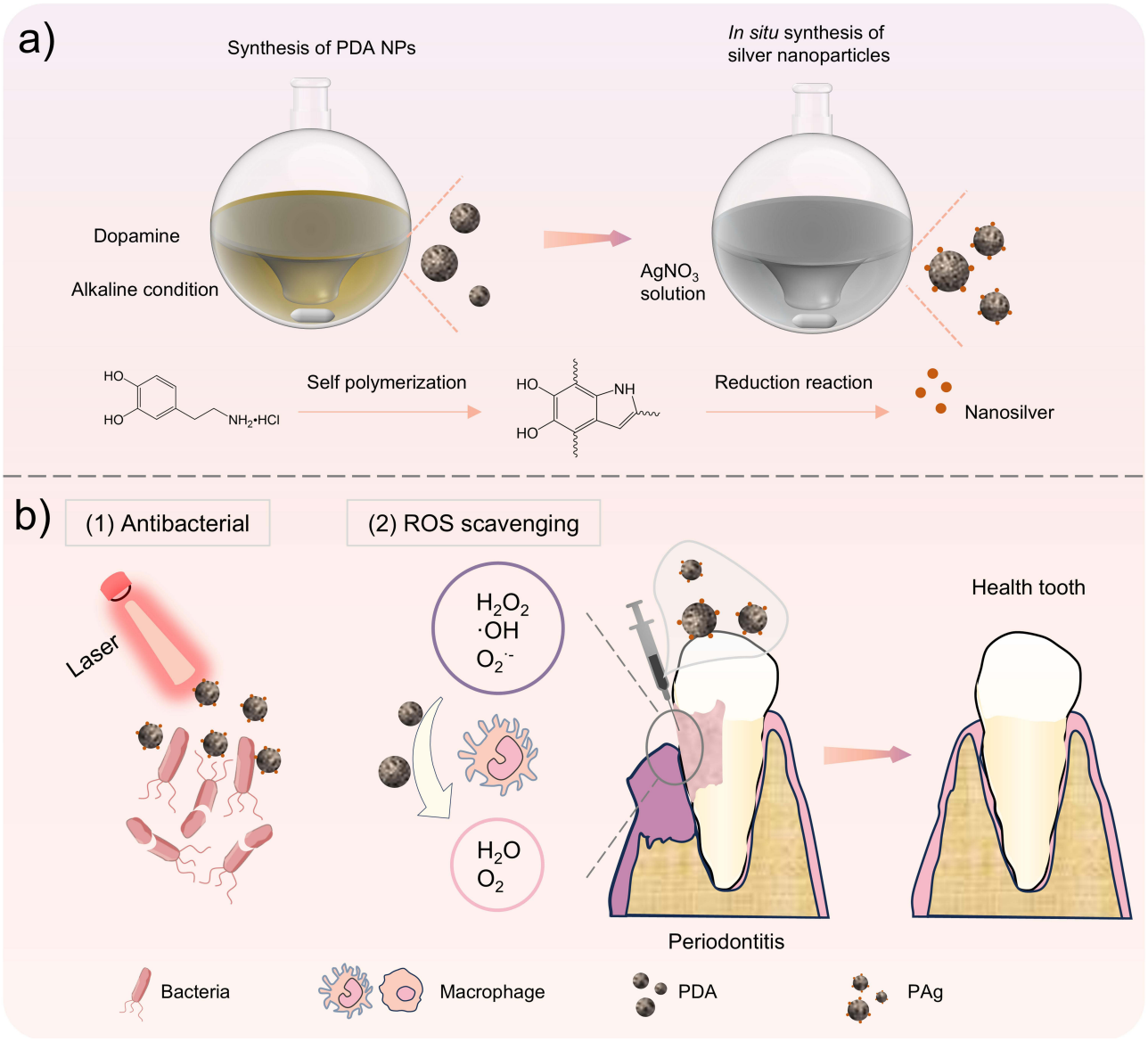

improving the treatment outcome.[10,11] Therefore, finding appropriate strategies to improve the periodontal microenvironment and alleviate inflammatory responses is of great significance for the therapy of chronic periodontitis.

Currently, nanomedicine carriers have attracted much attention due to their size-induced unique advantages and multifunction.[12,13] Firstly, the nanoscale has a large specific surface area, which is more conducive to contact with bacteria and does not occupy the growth space of osteoblasts and fibroblasts.[14] Secondly, there is a positive antibacterial advantage, such as the efficient antibacterial property of precious metal ions.[15,16] Thirdly, they have good biocompatibility and stimulate the growth and differentiation of osteoblasts.[17] Considerable effort has been dedicated to the synthesis of various new nanoparticles aimed at the continuous eradication of periodontal bacteria or the elimination of ROS.[18] Despite the rapid progress in the design of various novel nanocarriers, which are mainly used for the eradication of dental plaque, these therapeutic strategies still encounter some problems, such as limited antibacterial efficacy and low anti-inflammatory activities. While significant efforts have been devoted to periodontal nanotherapeutics, current systems remain constrained

by functional compartmentalization. Monofunctional antibacterial platforms (eg, the minocycline gel used in clinical practice) fail to address ROS-mediated tissue damage. Conversely, antioxidant-focused nanocarriers (eg, CeO_2 nanozymes scavenging ROS with negligible antibacterial action,[19] and locally delivered atorvastatin (2% w/v) containing chitosan formulations reducing IL-1β, IL-6, IL-8, IL-10[20]) permit biofilm recurrence. Emerging dual-functional systems such as Ag-MnO_2 requiring toxic H_2O_2 input for catalase-like activity,[21] still depend on robust triggers. Thus, the essential triad for curative periodontitis management contains physical biofilm disruption, enzymatic ROS scavenging, and regenerative microenvironment modulation.

Among various multifunctional nanomaterials, polydopamine nanoparticles (PDA NPs) and their derivatives exhibit exceptional near-infrared absorbance, robust chelating capacity for metal ions, and significant biocompatibility.[22–24] Consequently, they have been extensively utilized as photoacoustic contrast agents, photothermal agents (PAs), and biomedical chelating agents.[25] Furthermore, PDA-based materials, which are natural biopolymers, have shown their ability to neutralize free radicals from UV light, safeguarding the brain from damage due to ROS in ischemic stroke, and treating prostatitis-damaged sexual behavior.[26] Collectively, this evidence suggests that materials based on PDA, which are enhanced with reducing functional groups like catechol and imine, hold significant potential for the elimination of multiple ROS both in vitro and in vivo.[27] In addition, PDA NPs demonstrate exceptional photothermal conversion efficiency when exposed to near-infrared light, facilitating bacterial cleavage and eradication through mechanisms involving membrane disruption and protein denaturation.[28] Nonetheless, the efficacy of antimicrobial photothermal therapy (PTT) is contingent upon achieving hyperthermic conditions, typically exceeding 60 °C, which can result in significant adverse effects to adjacent healthy tissues. Recent studies have indicated that mild PTT, characterized by temperatures below 50 °C, could potentiate the antibacterial efficacy by mitigating thermal resistance[29] and synergistic treatment with other therapies.[30,31] Additionally, the mild localized photothermal stimulation can significantly enhance tissue regeneration at sites of bone defects.[32,33]

Notably, silver nanoparticles are highly effective antimicrobial agents.[34] Their adhesion to bacteria induces instability and damage to the cell membrane, increasing its permeability and resulting in the leakage of cellular contents, ultimately leading to death.[35,36] Furthermore, evidence suggests that silver nanoparticles could interact with sulfur-containing proteins in bacterial cell walls, causing structural damage and potentially leading to cell wall rupture.[37,38] These nanoparticles may also disrupt the respiratory chain by interacting with mercaptan groups in enzymes, thereby generating ROS and free radicals, which damage intracellular mechanisms and activate apoptotic pathways.[39] However, the bactericidal efficacy of silver nanoparticles is significantly diminished due to their propensity to aggregate, necessitating the development of a more stable nanosystem.

Herein, we proposed the development of an antioxidant defense platform with antibacterial properties, which employed PDA NPs as intelligent scavengers to mitigate ROS from oxidative stress in periodontitis and silver nanoparticles as a potent antibacterial agent to eliminate plaque biofilm. As illustrated in Figure 1, the construction of the fabricated nanoplatforms involves two primary steps: initially, well-dispersed PDA nanoparticles are synthesized through the self-polymerization of dopamine at alkaline condition, followed by the in situ reduction of silver ions to form nanoparticles on the surface of PDA facilitated by the polydopamine. One of the most intriguing features of the designed nanoplatforms is that the abundant functional groups on the surface of PDA not only ensure the excellent dispersion of PDA, but also reduce silver ions, which effectively avoids the aggregation of Ag nanoparticles. Additionally, the application of our designed nanoarchitecture was broadened by using PDA nanoparticles as the core, which offers the antibacterial photothermal therapy under NIR laser. Furthermore, NIR laser enhances ROS scavenging by boosting enzymatic activity through the stimulating reduction of PDA. In order to validate these, comprehensive experiments were conducted in vitro and in vivo rats. Moreover, the investigation focused on the photothermal conversion effect, enzyme-like activity in vitro, and the scavenging of cellular ROS to demonstrate anti-inflammatory potential.

Materials and Methods

Materials

Dopamine hydrochloride ($C_8H_{11}NO_2 \cdot HCl$), Tris (hydroxymethyl) methyl aminomethane ($C_4H_{11}NO_3$) and Tris (hydroxymethyl) methyl aminomethane hydrochloride were purchased from Aladdin Biochemical Technology Co., Ltd (Shanghai, China). Silver nitrate ($AgNO_3$), sodium chloride (NaCl), and dimethyl sulfoxide (DMSO) were obtained from Sinopharm Chemical Reagent Co., Ltd (Shanghai, China). The 3-(4,5-dimethylthiazol-2-yl)-2,5-diphenyltetrazolium bromide (MTT),

 https://doi.org/10.2147/IJN.S533622

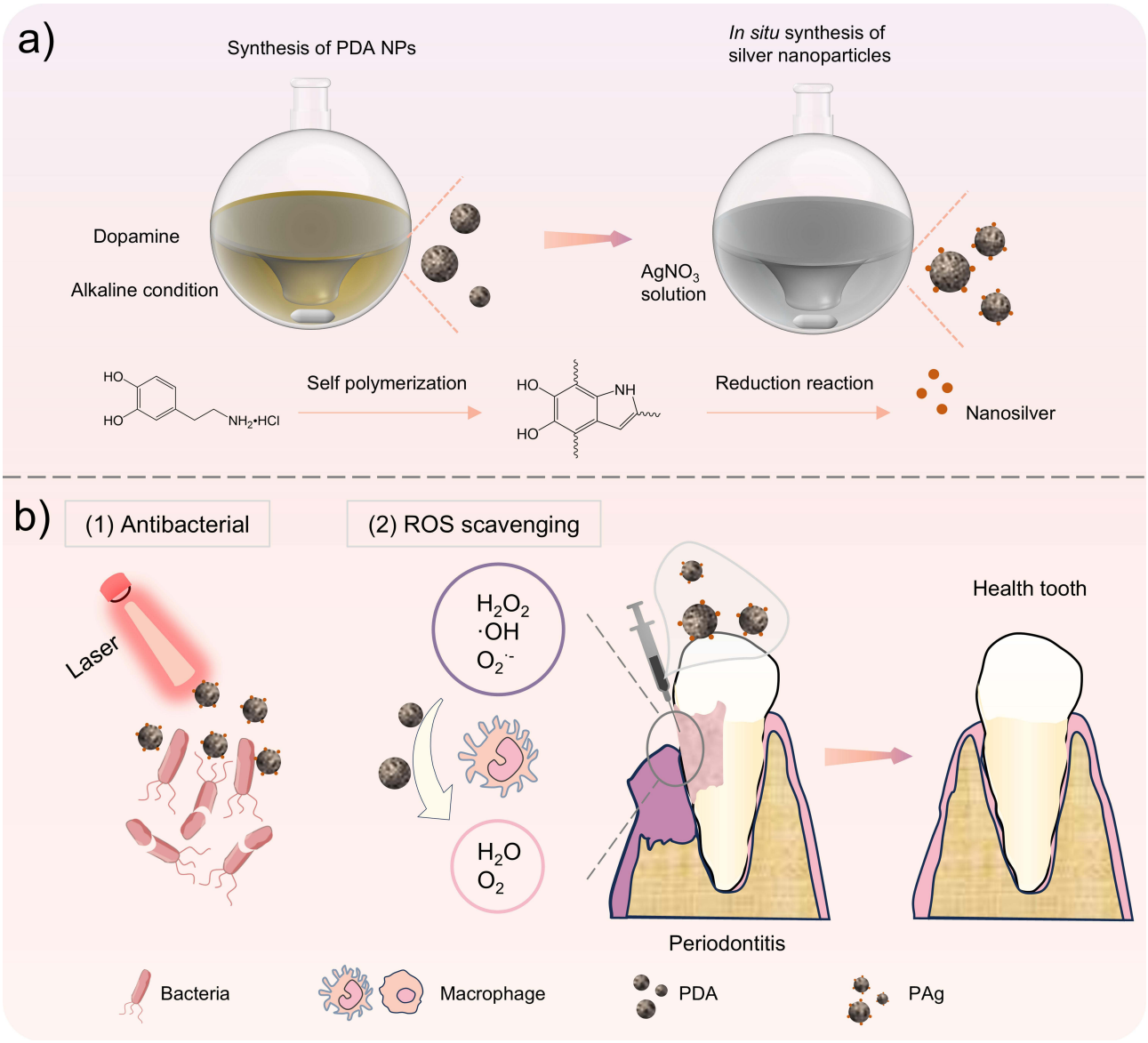

Figure 1 Schematic of (**a**) the step-by-step synthesis of the fabricated PAg by self-polymerization of dopamine and reduction of Ag ions, and (**b**) the therapeutic mechanism for periodontitis from the design of nanocomposites.

CCK-8 kit, hematoxylin and eosin (H&E), SOD assay kit were obtained from KeyGen Biotechnonoly Co., Ltd (Nanjing, China). Hemin, Live/Dead cell staining kit, and crystal violet were purchased from BASF Bio-Tech Co., Ltd (Hefei, China), UElandy Inc. (Suzhou, China), and Biosharp (Guangzhou, China), separately.

The Preparation of PAg

To prepare PDA, a classical Stöber method with the modifications was used according to the reports.[27] Briefly, 2 mL NH·OH and 40 mL ethanol were mixed with 90 mL water, and then stirred for 0.5 h. Further, 10 mL dopamine hydrochloride solution (50 mg mL^{-1}) was added into the above mixture, and then stirred for 1 day to synthesize PDA. Finally, PDA was collected via centrifugation and washed with water.

PAg was prepared utilizing the reducibility of PDA to transform Ag^{+} to silver nanoparticles on the surface of PDA via the reduction reaction. Typically, PDA (1 mg) was dispersed into 10 mL of water. Further, 5 mL $AgNO_3$ solution (1 mg mL^{-1}) was added into the above solution and stirred (protected from light) for 1 h. PAg was collected via centrifugation and washed with water.

The Characteristics of PAg

The characteristics of PAg were measured according to the previous report.[40,41] The surface topography and micro-morphology of the fabricated nanocomposites were observed by scanning electron microscope (SEM, Hitachi SU8100, Japan) and transmission electron microscope (TEM, JEOL JEM-F200, Japan). The element distribution at PAg was detected by energy dispersive spectrometer (EDS) of TEM. Then, we used zeta sizer (Malvern Nano ZS90, English) to measure the size distribution and zeta potential of PDA and PAg. The absorption spectrums of the designed nanoparticles were estimated by Ultraviolet–visible (UV–Vis) spectrophotometer (V-670, Jasco, Japan). Further, the changes of chemical groups at the synthetic nanoparticles were evaluated by Fourier transform infrared spectrometer (FTIR, Thermo Fisher Nicolet iS50, US).

To evaluate the colloidal stability of PDA and silver-deposited PAg, they were suspended in three distinct media under standardized conditions: phosphate-buffered saline (PBS), fetal bovine serum (FBS), and artificial saliva (AS).[7] Their physical stability was assessed through visual observation and photographic documentation.

The Photothermal Effect of PAg

To estimate the photothermal conversion effect of the fabricated nanoparticles at near-infrared light, 1 mL PDA or PAg at various concentrations was added into cuvette and irradiated by 808-nm laser at 1 W cm^{-1}. The temperature was recorded by a thermal detector (HB DT1311, China). Moreover, to further evaluate the photothermal stability of the designed nanoparticles, PDA and PAg were irradiated repeatedly for 4 cycles and recorded the highest temperature change.

RO/NS-Scavenging Assessment

The peroxidase (POD)-like activities of PDA and PAg were measured by a 2,2'-azino-bis (3-ethylbenzthiazoline-6-sulfonic acid) (ABTS) method. Briefly, 50 μL 50 μg/mL nanoparticles, 50 μL 30% H_2O_2, and 150 μL 10 mg/mL ABTS were added into 1 mL water. After the chromogenic reactions for 10 min, the absorbance was recorded by a microplate reader (Infinite 200 Pro, Tecan, Austria).

The hydroxyl radical (•OH) scavenging capacity of PDA and PAg was evaluated using a Fenton reaction-based assay. In this method, •OH generated via the Fenton reaction oxidize terephthalic acid (TPA) to 2-hydroxyterephthalic acid (HTPA), which exhibits fluorescence. 2 mL of deionized water was added to a centrifuge tube, followed by the sequential addition of 50 μL of $FeSO_4$ solution (10 mg mL^{-1}), 10 μL of disodium terephthalic acid (NaTA) solution (10 mg mL^{-1}), and 100 μL of PDA or PAg solutions at varying concentrations (25, 50, 100, and 200 μg mL^{-1}). Finally, 10 μL of H_2O_2 (30%) was added to initiate the Fenton reaction. After 1 minute of reaction, the fluorescence intensity of HTPA was measured at an emission wavelength of 425 nm by a fluorescence spectrophotometer (Hitachi F-7000, Japan) with an excitation wavelength of 315 nm. The hydroxyl radical scavenging capacity was calculated based on the reduction in fluorescence intensity compared to the control.

The SOD-like activity of PDA and PAg was evaluated using a commercial Total SOD Activity Assay Kit (WST-8 method, Beyotime Biotechnology). This kit employs a colorimetric reaction based on WST-8 to quantify superoxide dismutase (SOD) activity in samples. Briefly, 20 μL of PDA or PAg solutions at varying concentrations (25, 50, 100, and 200 μg mL^{-1}) were added to a 96-well plate, followed by the addition of 160 μL of WST-8/enzyme working solution and 20 μL of reaction initiation working solution. The plate was incubated at 37 °C for 30 minutes. The absorbance at 450 nm was measured using a microplate reader, and the SOD-like activity was calculated based on the absorbance values.

The catalase (CAT)-like activity of PDA and PAg nanoparticles was evaluated by measuring their ability to catalyze the decomposition of hydrogen peroxide (H_2O_2) into oxygen (O_2). The oxygen concentration in the solution was quantified using a dissolved oxygen meter (JPBJ-608, Leici, China). Briefly, 6 mL of phosphate-buffered saline (PBS, pH 7.4) was added to a 50 mL centrifuge tube, followed by the addition of 2 mL of H_2O_2 solution (30%) and 2 mL of nanoparticle suspension (200 μg mL^{-1}). The oxygen concentration was recorded over time, and the data were plotted to assess the catalytic activity.

For the 1,1-Diphenyl-2-picrylhydrazyl radical 2,2-Diphenyl-1-(2,4,6-trinitrophenyl) hydrazyl (DPPH) scavenging ability, the reaction was recorded by a microplate reader (Tecan Infinite 200 Pro, Austria). PDA and PAg with the

concentration 0, 12.5, 25, 50, 100, 200 μg mL^{-1} were mixed with DPPH in ethyl alcohol (100 μL, 0.1 mM) and measured by a microplate reader.

Cellular ROS Scavenging

To mimic the periodontitis microenvironment, lipopolysaccharide (LPS) was utilized to stimulate Raw 264.7 cells and human periodontal ligament cells (HPLCs) for producing excessive ROS. Briefly, Raw 264.7 cells and human periodontal ligament cells (HPLCs) were seeded into 24-well plates incubating overnight. Then, cells were pre-incubated with PDA (25 and 50 μg mL^{-1}) for 4 h, and then added LPS (1000 ng mL^{-1}) for stimulation. After 4 h, the cellular ROS was detected by ROS assay kit. Finally, it was observed by fluorescence microscope (Leica DMi8, Germany).

Biocompatibility

Briefly, cells were seeded into 96-well palate for overnight, and then added PDA with different concentrations (25, 50, 100, 200, 400 μg mL^{-1}). After incubating for 24 h, CCK8 was added to the kit and incubated for 2 h. Then, the absorbance was measure at 450 nm by a microplate reader (Tecan Infinite 200 Pro, Austria). Accordingly, AO/EB live/dead double staining kit was used to investigate the growth state of cells after incubating with PDA. Then the images were observed by a fluorescence microscope.

Further, the hemolysis test of the designed nanoparticles was also investigated. Initially, rat blood was collected and red blood cells were collected by centrifugation. Then red blood cells were incubated with PDA at different concentration (25, 50, 100, 200, 400 μg mL^{-1}) for 4 h at 37 °C. Finally, the supernatant was collected by centrifugation, the absorbance was measured by a UV–Vis spectrophotometer, and the hemolysis ratio was calculated.

In vitro Sterilization

Planktic-Bacterial Sterilization Assessment

To assess the antibacterial capability of the designed nanocomposites, briefly, *Porphyromonas gingivalis (P. gingivalis)* solution was treated by PAg (200 μg mL^{-1}) under the irradiation of 808 nm laser at 1.5 W cm^{-1} for 10 min. After incubating with PAg for 6 h, *P. gingivalis* were diluted for different times and spread on brain heart infusion (BHI) agar plate. Then colony-forming units (CFU) were counted after growth for 3 days.

The 0.5 mL *P. gingivalis* solution was added into 0.5 mL PAg. After treatments with PAg and laser irradiation and then incubation for 6 h, *P. gingivalis* were centrifuged and washed with normal saline twice. The *P. gingivalis* were stained with live/dead bacterial staining kit, and the observed and recorded by fluorescence microscope.

The *P. gingivalis* were seeded into 96-well plate, and added PAg under irradiation for 10 min. After incubation for 6 h, 20 μL methyl thiazolyl tetrazolium (MTT) were added. Then, optical density (OD) was detected by microplate reader at 490 nm after incubating for 1 h at bacterial incubator and calculated the bacterial viability rate.

Anti-Biofilm Assessment

To obtain biofilm, *P. gingivalis* were seeded into 48-well plate for 4 days to form biofilm. Then, PAg (400 μg mL^{-1}) was added and irradiated with 808-nm laser. After treatments, biofilms were sonicated to disperse the bacteria, and spread BHI ager plate. After 2 days incubation, CFU was counted. In addition, crystal violet staining was also used to evaluate the anti-biofilm capacity of PAg. After treatments, sterile water gently washed biofilm. Then, the 0.1% crystal violet solution was stained for 30 min. The excess crystal violet of biofilms was washed with abundant water. The 2 mL 95% ethanol was used solve crystal violet, and the absorbance was measured at 570 nm by microplate reader. Finally, the bacterial viability rate was calculated.

The viability of bacteria was assessed using a commercial live/dead bacterial viability kit, which contains two fluorescent dyes, NucGreen and Ethidium Homodimer-III (EthD-III), to distinguish between live and dead bacteria. *P. gingivalis* were seeded on HA disks for 4 days. Briefly, following various treatments, 1.5 μL of NucGreen and 1 μL of EthD-III were mixed with 7.5 μL of 0.85% NaCl solution to prepare the staining working solution. A 5 μL aliquot of the staining solution was applied to the hydroxyapatite discs containing bacterial biofilm. After incubation in the dark at

room temperature for 15 minutes, the biofilms were imaged by a confocal laser scanning microscope (CLSM, FV3000, Olympus, Japan).

In vivo Therapeutic Assessment

All animal experiments complied with the Chinese guidelines for the Ethical Review of Welfare of Laboratory Animals (GB/T 35892–2018) and the Animal Ethics Committee of Nanchang University (No. NCULAE-20221228041). After successfully modeling through ligation method, Wistar rats were randomly divided into three groups: periodontitis, PAg, PAg + Laser (L). Severally, rats with periodontitis were chosen as the positive control and were injected with 100 μL PBS during treatment. PAg group was injected with 100 μL PAg (10 mg mL^{-1}). PAg +L group was injected with 100 μL PAg (10 mg mL^{-1}) and irradiated with 808-nm laser for 10 min. Besides, healthy rats were chosen to negative control. During the laser irradiation process, the temperature changes in the periodontal tissue were monitored and recorded using an infrared thermal imaging camera. Real-time thermal images were captured to assess the photothermal effect induced by the 808 nm NIR laser.

After treatments, all rats were sacrificed, and gingival tissues were harvested from the rats and preserved in RNALater™ Stabilization Solution to maintain RNA integrity. The tissues were homogenized, and total RNA was extracted for subsequent PCR analysis (TNF-α, IL-1β, IL-6). Additionally, gingival tissues were flash-frozen in liquid nitrogen, homogenized, and subjected to protein extraction for Western blot (WB) analysis.

For histological examination, gingival tissues were fixed in glutaraldehyde, embedded in paraffin, and sectioned. The sections were stained with hematoxylin and eosin (H&E) for morphological evaluation. Furthermore, immunohistochemical (IHC) staining was performed to detect specific antigens. The intensity of positive staining in IHC depends on the antigen content, distribution density, and the sensitivity of the labeling method.

Statistical Analysis

All data were expressed as the mean ± standard deviation ($n \geq 3$). The statistical significance of the data was calculated via a one-way analysis of variance, followed by Tukey's test. A p-value of < 0.05 was considered statistically significant (*$p < 0.05$; **$p < 0.01$; ***$p < 0.001$).

Results and Discussions

Physicochemical Characteristics

The synthesis of the PDA NPs reliably based on the self-polymerization of dopamine according to the previous reports.[27,42] The aggregation of PDA polymer formed nuclear and further nanoparticles as the reaction proceeded with a sufficient concentration. Simultaneously, the color of mixture solution changed from transparency to black, may contributing to the absorption for light and photothermal effect. After fabrication, the uniform size of PDA nanosphere was about 150 nm from SEM and TEM images (Figure S1), and the surface was smooth. Further, the particular self-polymerization did keep the abundant functional group, giving the chance to reduce Ag ion without adding other reductants, and strongly attracted silver nanoparticles which should attributing the chelation of catechol for metal.[43] As displayed in Figure 2a and b, the surface and structure morphologies were investigated according to SEM and TEM images. The little and fewer pots (Ag NPs ~5 nm) were observed to be symmetrically dispersed on the surface of PDA, which may contribute to the rapid Ag^{+} release from the designed nanofabrication and reduce the toxicity in the application. In addition, the element distribution in PAg was observed from the results of TEM mapping (Figure 2c), which N, O elements distribute at the core and Ag atom distributed at the surface. Moreover, the ratio of elements is shown in Table 1, and Ag atom content was approximate 1.6%. It was noted that the ratio between PDA polymer to Ag atom was about 35:1 after calculation, indicting less Ag content at the designed PAg.

Further, to investigate the properties of our fabricated nanocomposites at the colloid status, the size distribution, zeta potential and stability of the designed nanofabrication were measured by dynamic light scattering (DLS). As displayed at Figure 2d, the hydrated sizes of PDA and PAg at aqueous solution were about 174 nm and 194 nm, ranging from 170 to 180 nm, 192 to 196 nm, respectively. In addition, the polydispersity indexes (PDI) of PDA and PAg were approximately 0.05 and

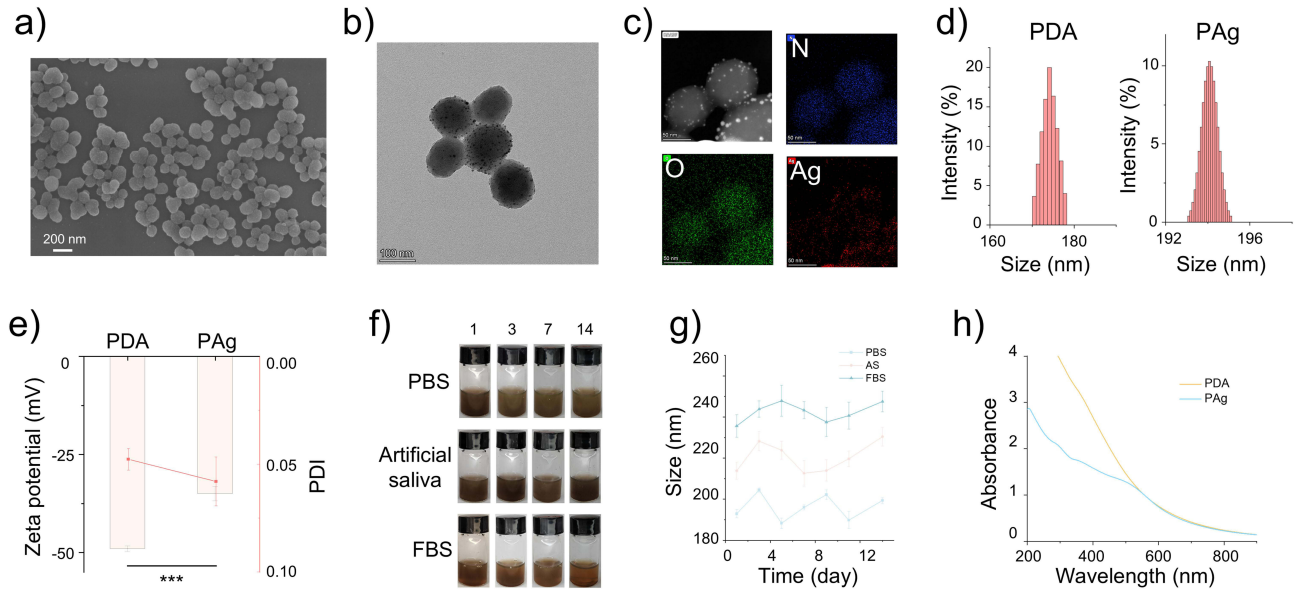

Figure 2 The physicochemical characteristics of the designed nanocomposites. (**a**) SEM and (**b**) TEM images of PAg. (**c**) Mapping of PAg, N, O, Ag elements. (**d**) The size distribution, (**e**) Zeta potential and PDI of PDA and PAg. (**f**) The photographs and (**g**) the size changes of PAg dispersed at PBS, artificial saliva and FBS for 14 days to observe stability. (**h**) UV-Vis-NIR absorption spectra of PDA and PAg. ***P < 0.001.

0.06 < 0.1 (Figure 2e), suggesting the narrow distribution, monodispersed and uniform size, corresponding to SEM and TEM images (Figure 2a and b). In addition, a litter increasement of size presented after synthesis of Ag NPs, indicating the effective chelation with PDA. Besides, the Zeta potential of PDA and PAg in aqueous solution altered from −48 mV to −35 mV (Figure 2e), which indicated the good colloid stability from the surface electrostatic repulsion of the amidogen and hydroxyl. Then, for estimating the colloid stability at various solution, PDA and PAg were dispersed into PBS, artificial saliva (AS), FBS to observe and record the status for 14 days (Figures 2f and S2). Moreover, the size variations of PDA and PAg were also recorded by DLS (Figures 2g and S3). The reduction of Ag NPs may break the surface electric double layer to aggregate at the media. It is noted that no agglomeration emerged during the process of 14 days with the release of Ag^+ from PAg. Prominently, the colloid dispersity and stability play key roles on the biomedical application for the nanocomposites. It is known that PDA have excellent colloid dispersity and stability at aqueous solution,[25] but the different media (such as high protein and hypersaline solution) also performed well, which could be attributed to the plenty of functional groups presenting electrostatic repulsion with protein and salt. In addition, the results demonstrate the Ag NPs have a little effect for surface, which may attribute to the low content on the shell of PDA from our design. It could help enhance the stability of Ag NPs without any modification for silver.

To further indicate the surface and inner properties, UV-Vis-NIR spectra were evaluated as shown in Figure 2h. It showed that PDA nanoparticles exhibit broad-spectrum absorption across the UV-Vis-NIR range (200–900 nm), attributed to their π–π conjugated structures and polyphenol-quinone chromophores. It is notable that upon in situ synthesis of silver nanoparticles (Ag NPs) on PDA surfaces, a significant reduction in UV-region absorption (200–400 nm) was observed, accompanied by the emergence of a localized surface plasmon resonance (LSPR) band near 400 nm, characteristic of Ag NPs.[44] The UV-region

Table 1 The Different Atomic Rate-Based EDS of PAg

Element	Atomic %
N	55.60
O	42.80
Ag	1.61

attenuation may arise from two synergistic mechanisms: (1) Competitive LSPR absorption and interfacial charge transfer. The electron transfer from Ag NPs' conduction band to PDA's valence band suppressed π–π* transitions in PDA (200–350 nm), collectively diminishing UV absorption; (2) Surface oxidation-induced structural perturbation. The catechol groups on PDA were oxidized to quinone structures during Ag^{+} reduction to Ag NPs, disrupting localized π–π conjugation network, thereby weakening short-wavelength UV absorption (200–300 nm). Concurrently, the composite demonstrates enhanced feasibility for NIR photothermal applications. PDA dominates NIR absorption (700–900 nm) due to its intrinsic π–π* transitions and quinone-related narrowband absorption, amplified by light scattering and internal multiple reflections in 100 nm PDA particles. Although Ag NP exhibit no direct NIR absorption, they indirectly enhance photothermal efficiency via acting as high-thermal-conductivity mediators to accelerate heat dissipation from PDA, mitigating efficiency losses caused by thermal localization.

Photothermal Effect to Mild PTT for Periodontitis

To further observe the photothermal effect of the hybrid nanoplatforms after integrating Ag nanoparticles, PAg colloid solution was directly irradiated by NIR laser for 10 min at 1.5 W cm^{-1}, and the temperature variation was immediately recorded. Comparing with water as control, the temperature of PDA and PAg significantly elevated at various concentrations (50, 100, 200, 300, 400 μg mL^{-1}) at the irradiation of 808-nm laser (Figures 3a and S4). Moreover, the temperature changed smaller with the higher concentration, may attributing to the limited photothermal conversion efficiency and the rapid heat exchange with the environment. The thermal images of 1 mL PAg aqueous solution (200 μg mL^{-1}) at cuvette were recorded from 25 to 50 °C for 10 min (Figure 3b), also indicating the significant photothermal conversion efficiency. Notedly, the temperature comparison between PDA and PAg demonstrated that the reduction of Ag NPs does not impact the π-electron clouds mainly facilitating the photothermal effect at PDA. In addition, to evaluate the photothermal stability, the absorption spectra of PDA and PAg were observed before and after laser irradiation and the

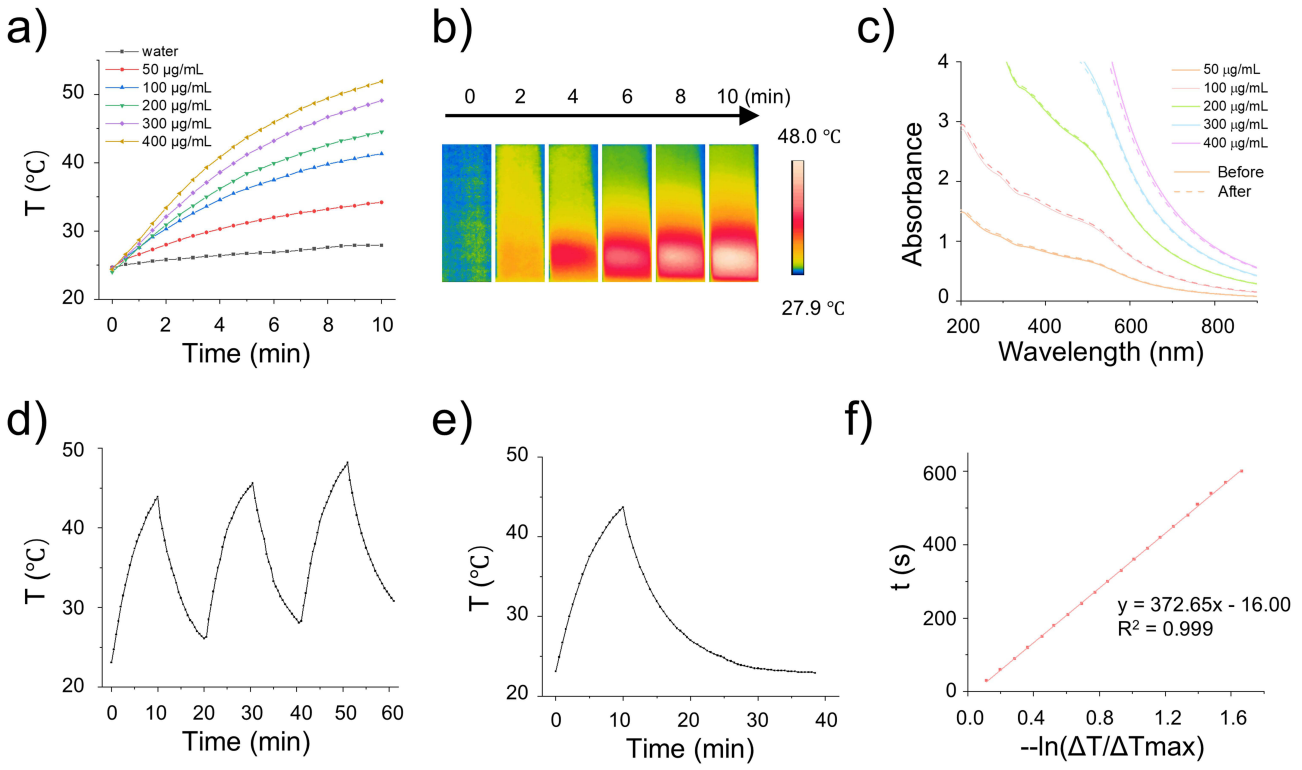

Figure 3 The photothermal effect and stability of PAg. (**a**) The temperature variation of PAg with different concentration at the irradiation of 808-nm laser with 1.5 W cm^{-1} for 10 min. (**b**) The thermal images of PAg at 200 μg mL^{-1} at the irradiation for 10 min. (**c**) UV-NIR absorption spectra of PAg before and after the laser irradiation. (**d**) The 3 recycle laser irradiation for PAg at 200 μg mL^{-1}. (**e**) The temperature rise and descend curve of PAg at the irradiation of 808-nm laser for 10 min and no laser irradiation. (**f**) The fitting line of PAg cooling.

https://doi.org/10.2147/IJN.S533622

photothermal recycle was assessed. As shown in Figure 3c, the absorption curve did not obviously change at various concentrations. Besides, the temperature sustainedly increased at the three recycles for 20 min (Figure 3d). Consequently, the structure of PDA kept integrity under the irradiation due to the photothermal mechanism.[25] To precisely analyze the photothermal effect, the photothermal conversion efficiency of PAg was ~22.3% through calculation by the formula (Figure 3e and f). Comparison with other photothermal agents such as carbon materials,[45] metal materials,[46] small molecular materials,[47] the photothermal conversion efficiency of PAg is not dominant, but it is also sufficient in the treatment of periodontitis, because it prevents the hyperthermia in PTT from damaging the normal tissue.

Light exhibits wave-particle duality, endowing it with both penetrating capabilities and a quantifiable amount of energy. Consequently, phototherapy is extensively employed in the treatment of various diseases, including photodynamic therapy (PDT) and PTT, for conditions such as skin disorders,[48] cancer treatment,[49] and so on. Additionally, phototherapy also possesses antimicrobial properties, rendering it effective for the treatment of several infectious diseases, including periodontitis. Some studies have explored the development of diverse materials to enhance PDT for periodontitis,[50] including the incorporation of supplemental oxygen to address hypoxia in periodontal tissues. Focusing on another aspect of phototherapy, photothermal therapy also exhibits antibacterial properties. However, a significant challenge is that it requires elevated temperatures to effectively eradicate bacteria, which poses a risk of damaging healthy tissues. Therefore, optimizing photothermal therapy involves reducing the operational temperature to improve its clinical applicability. The primary limitation of low-temperature photothermal therapy lies in its slow energy accumulation process. This modality necessitates achieving effective treatment of pathological tissues at relatively low temperatures, thereby requiring a more gradual and sustained photothermal conversion process. Consequently, the therapeutic efficacy may be constrained, as the relatively low temperatures employed may not suffice for killing bacteria, leading to suboptimal treatment outcomes. Nonetheless, a notable advantage of low-temperature photothermal therapy is its capacity to mitigate inflammation, as the reduced temperatures can diminish the excessive inflammatory response typically associated with hyperthermia. To achieve therapeutic efficacy, low-temperature PTT can be integrated with other treatment modalities, as the synergistic effects of these combined approaches ensure the optimal performance of low-temperature PTT. In this study, we designed a strategy that combines silver nanoparticle-based therapy with low-temperature PTT, thereby enhancing the therapeutic outcomes of low-temperature photothermal treatment.

ROS/RNS Scavenging

Given that excess ROS/RNS from the inflammatory reaction breaks normal tissue, the effective ROS/RNS scavenger plays a vital role in reversing the immune imbalance to efficiently cure periodontitis[51,52] Polydopamine has weak reducibility due to its catechol, but whether PDA nanoparticles and modified PDA nanoparticles have enzyme-like activity and which enzyme activities need to be further explored. To investigate the ROS scavenging capacities and the enzyme activities of the designed nanocomposites, three ordinary ROS (H_2O_2,·OH,$\cdot O_2^-$) from the respiratory chain were utilized to react with PDA and PAg nanoparticles. Initially, H_2O_2 as the most common ROS was eliminated through transforming to H_2O from the catalysis of POD and CAT. The POD-like activity of the designed nanocomposites was measured by ABTS method, whereas there is no noticeable change on the process comparing with the control group (Figure 4a), indicating PDA and PAg have no POD-like activity. In addition, CAT-like activities of PDA and PAg were evaluated by monitoring the dissolved oxygen with the catalysis H_2O_2. As shown in Figure 4b, lots of O_2 bubble from the decomposition of H_2O_2 adhered to the walls of the centrifuge tubes comparing with control group (no obvious bubbles). Moreover, the dissolved oxygen only increased approximately 1 mg mL^{-1} at control group, ~ 8 and 7 mg mL^{-1} at PDA group and PAg group for 20 min. The initial CAT-like catalytic rates of PDA and PAg were 1.52 and 1.3 mg L^{-1} min^{-1}, respectively, almost the same as the result of the early report.[53]

To further estimate SOD-like and ·OH scavenging activities of the fabricated nanocomposites, PDA and PAg were added into the reaction system which generated O_2^- and OH, respectively. Herein, the superoxide anion (O_2^-) produced by xanthine/hypoxanthine under the catalysis of xanthine oxidase oxidized WST-8 to produce water-soluble formazan dye. The O_2^- scavenging rate of PDA and PAg reached to about 50% at the concentration of 200 μg mL^{-1} (Figure 4c) through calculating the colorimetric analysis of WST-8 products, demonstrating that the fabricated nanocomposites presented good SOD-like activity. Moreover, it should be observed that the residual rate of PAg was a little higher than that of PDA, suggesting that Ag

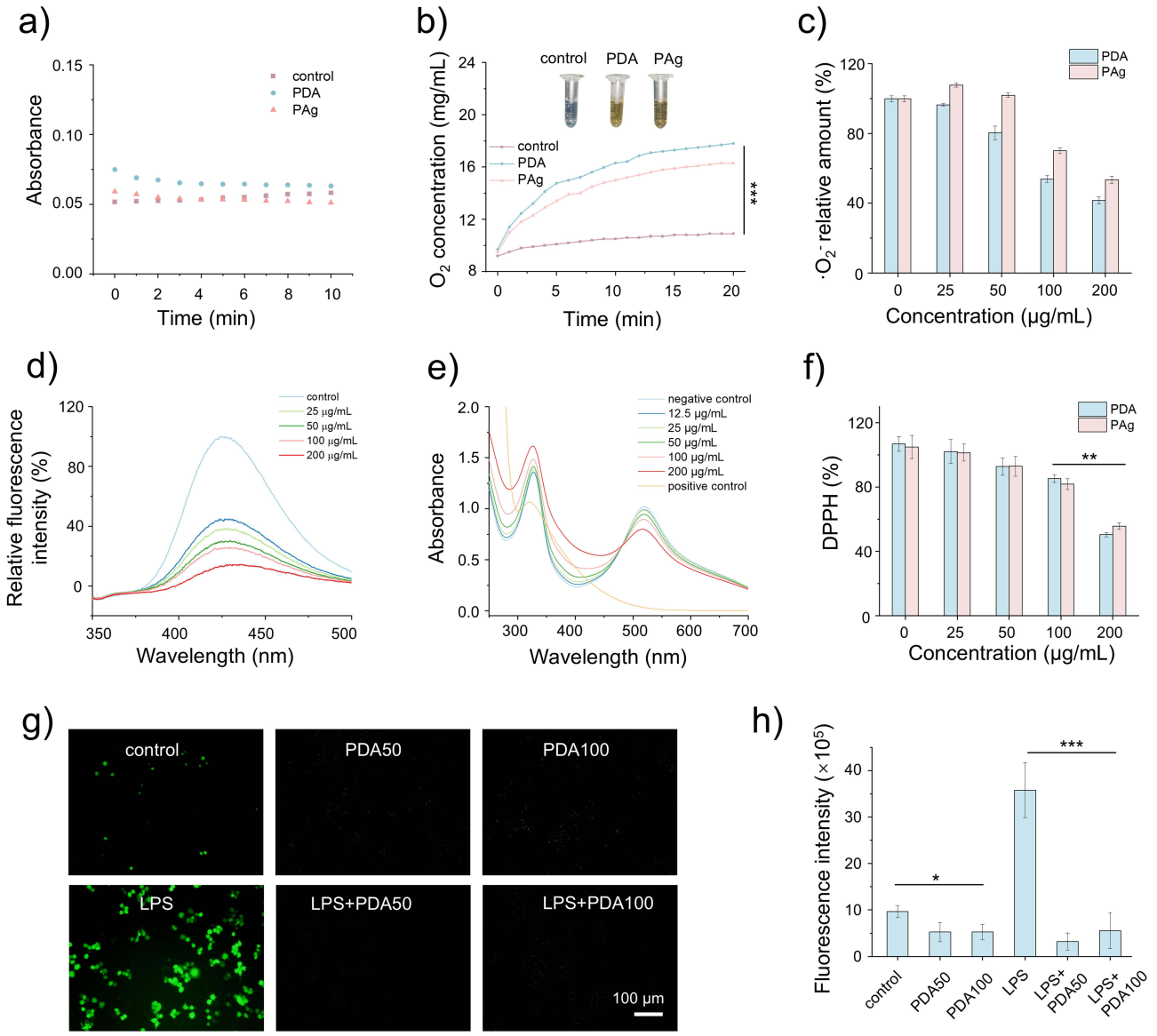

Figure 4 The RO/NS scavenging assessment of the designed nanocomposites. (**a**) POD-like activity. The absorbance of oxATBS with the catalysis of PDA and PAg at 645 nm wavelength. (**b**) CAT-like activity. Dissolved O_2 concentration of the reaction solution which PDA and PAg (200 μg mL^{-1}) mixing with H_2O_2 at PBS. (**c**) SOD-like activity. $\cdot O_2^-$ relative amount after the reaction through the catalysis of PDA and PAg by WST-8 method. (**d**) ·OH scavenging. The relative fluorescence spectrum of oxTA after eliminating ·OH by PAg at various concentration. (**e**) The absorbance spectrum of DPPH after treating with PAg at various concentration. (**f**) DPPH relative content after incubating with PDA and PAg. (**g**) The fluorescence images and (**h**) intensity of Raw264.7 after different treatments. *P < 0.05, **P < 0.01, ***P < 0.001.

may influence the SOD-like activity.[54,55] In addition, the hydroxyl radical oxidation of TPA to HTPA was used to detect the hydroxyl radical scavenging ability of PDA and PAg. It was observed that the fluorescence intensity of HTPA clearly declined once PDA and PAg at low concentration (25 μg mL^{-1}), and sustainedly fell with the increased concentration ranging from 25 to 200 μg mL^{-1} (Figures S5 and 4d), indicating their ·OH scavenging activities as nanozymes.

Apart from popular ROS, reactive nitrogen species (RNS) are also the common free radical in vivo, which can cause a variety of inflammatory diseases, including periodontitis.[56,57] Moreover, an excess of RONS means that oxidative stress is increased in the periodontal tissues, which induces and exacerbates the inflammatory deterioration.[52] To evaluate the RNS scavenging of the fabricated nanoplatforms, DPPH as a stable nitrogen-centered radical appearing as a dark purple color was utilized to mixture with PDA and PAg. Upon reaction with antioxidants, the DPPH radical solution undergoes a gradual decolorization accompanied by a reduction in absorbance at 520 nm, a phenomenon that serves as an indicator for evaluating the antioxidant activity of a given sample.[26] As displayed in Figure S6, the color distinctly got lighter after

https://doi.org/10.2147/IJN.S533622

reacting for 30 min with PDA and PAg at various concentration. In addition, it is evident that absorbance significantly decreases as concentration increases through comprehensive wavelength scanning (Figures S7 and 4e). Moreover, quantitative analysis further elucidates the clearance rates of about 50% at 200 μg mL^{-1} (Figure 4f), suggesting that the designed nanocomposites are effective in removing both ROS and reactive nitrogen species (RNS). Additionally, the incorporation of nano silver does not affect the reducibility of PDA, aligning with experimental findings regarding ROS clearance. In conclusion, the RNS scavenging properties underscore the potential of PDA nanoparticles for future applications.

In virtue of the prominent scavenging effectiveness for ROS and RNS at the physiochemical level, cellular level also was further assessed by coculturing with PDA. After the uptake PDA, LPS was added to stimulate the oxidative stress of Raw264.7 and HPLCs. 2',7'-Dichlorodihydrofluorescein diacetate (DCFH-DA) undergoes hydrolysis by intracellular esterase to yield DCFH, which can subsequently be oxidized by ROS to generate the fluorescent compound DCF.[7] Therefore, DCFH-DA was utilized to evaluate the scavenging capability by measure the fluorescence. As displayed in Figures S8 and 4g, strong green fluorescence emerged at LPS group, indicating the effective stimulation for generating ROS and RNS. After successful uptake of PDA, the fluorescence obviously decreased a lot, suggesting that PDA not only has a strong ability to clear ROS and RNS from physicochemical environment, but also plays a strong role in the interior of cells. In addition, the quantitative fluorescent intensity of the 6 groups was quite different (Figures S9 and 4g), indicating that DCFH was not oxidized into fluorescent DCF in the cell. These results indicate that PDA can maintain its ability to clear ROS and RNS after endocytosis, which lays a foundation for the effective application of PDA.

ROS has a dual role. Under normal conditions, it aids in cell functions like proliferation and apoptosis, helping maintain cell balance. In periodontitis, pathogen invasion activates immune responses, leading to increased ROS and RNS production to kill pathogens.[52] However, excess ROS can damage cells, cause dysfunction or death, and exacerbate inflammation, creating a vicious cycle that damages periodontal tissues, including bone loss and ligament degradation. Traditional antioxidants like vitamin C and vitamin E are quickly metabolized in the body, resulting in a short action time.[58,59] They are rapidly absorbed and distributed, making it challenging to maintain effective concentrations in periodontitis lesions. This necessitates frequent dosing to sustain their antioxidant effects. PDA have unique structural advantages, with phenol hydroxyl groups that continuously react with and remove ROS.[26] Once delivered to a periodontitis site, they remain stable and provide long-term antioxidant effects, addressing excessive ROS and reducing the "blank period" from rapid drug metabolism. Additionally, their surface can be modified to attach antibacterial agents, enabling them to inhibit bacterial growth while removing ROS.

In vitro Sterilization

In light of the common causative organisms of periodontitis, *Porphyromonas gingivalis* (*P.g*) was chosen as a representative bacterium to assess the antibacterial efficacy of our synthesized nanocomposites, which are implicated in the pathogenesis and progression of periodontal disease. Beyond examining the anti-biofilm properties, the anti-planktonic bacterial activity of PAg was evaluated using the MTT assay, colony counting method, and bactericidal time–kill curve analysis. As illustrated in Figure 5a, bacterial growth inhibition exhibited a dose-dependent increase across various drug concentrations. At a concentration of 100 μg mL^{-1}, bacterial growth inhibition was observed at 20%. However, when the concentration was elevated to 200 μg mL^{-1}, the inhibition rate markedly increased to 70% with the application of near-infrared (NIR) laser. It indicates that PAg nanoparticles exhibit substantial antibacterial activity in conjunction with NIR light, effectively suppressing bacterial growth and proliferation. It is noted that the NIR thermal imaging results (Figure 5b) showed that the maximum temperature of laser irradiation (~50°C) was lower than 60°C. In addition, the three colonies were photographed and counted (Figure 5c) after overnight growth. Compared with the control group, the colony-forming units (CFU) in the PAg group were significantly much lower, indicating that our fabricated nanoplatforms had significant antibacterial ability and silver ions were released in large quantities from the PAg. On the contrary, the antimicrobial effect of NIR laser irradiation had little impact because the antimicrobial PTT temperature was low and not enough to kill the bacteria.[60] Furthermore, the quantification of CFU also showed that the number of colonies in the PAg group decreased to 10^4 compared to the control group. In contrast, the number of colonies in the control group remained at 10^8 (Figure 5d).

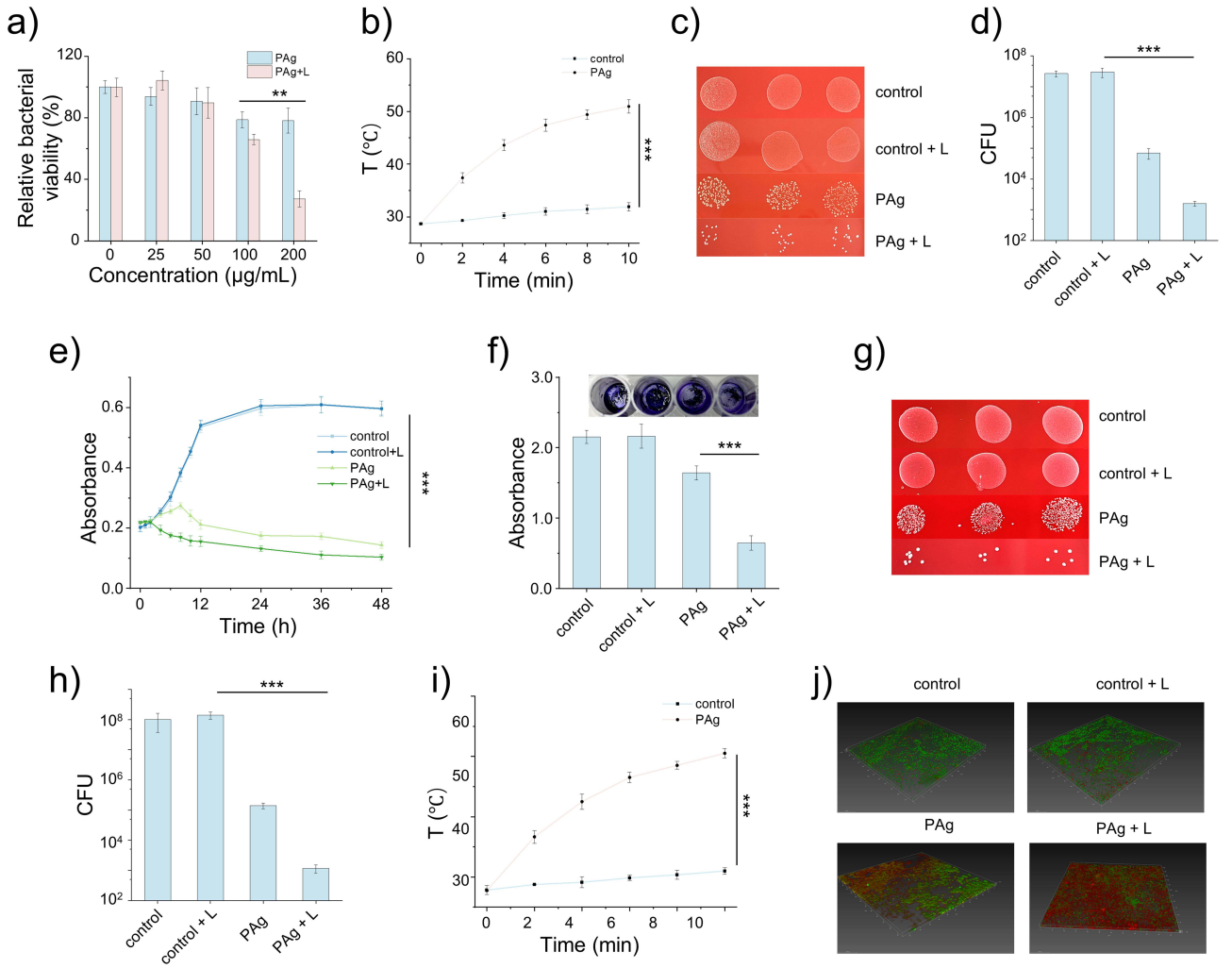

Figure 5 In vitro antibacterial and anti-biofilm evaluation of PAg for *P. gingivalis*. (**a**) MTT results for various concentrations under the irradiation of NIR laser. (**b**) The temperature variation of planktonic bacteria treating with PAg under the irradiation of 808-nm laser. (**c**) The colony formation images and (**d**) CFU counts of planktonic *P. gingivalis* after treating with PAg and PTT. (**e**) The bacterial growth curve of *P. gingivalis* after treating with PAg and PTT. (**f**) The crystal violet, (**g**) the colony formation images and (**h**) CFU counts of *P. gingivalis* biofilm after treating with PAg and PTT. (**i**) The temperature variation of biofilm growth in HA disk incubating with PAg under the irradiation of 808-nm laser. (**j**) CLSM images of biofilms at the surface of HA disks. **P < 0.01, ***P < 0.001.

To evaluate the prolonged bactericidal efficacy of the synthesized nanocomposites, the growth kinetics of *P.g* treated with PAg nanoparticles (NPs) were assessed by monitoring absorbance at 600 nm over various time intervals (Figure 5e). The control group exhibited a conventional bacterial growth curve. In contrast, the PAg-treated group demonstrated a slow bacterial growth rate within the first 6 hours, followed by a gradual decline and stabilization after this period. Notably, bacterial proliferation in the PAg group remained significantly low. The bactericidal activity of the nanoparticles was further enhanced upon the application of laser irradiation. The growth curve of *P.g* in the PAg group indicated sustained bacterial inhibition over a 48-hour period, as opposed to the increased absorbance observed in the control group. Initially, the interaction between the nanoparticles and the bacteria was weak; however, this interaction intensified over time, resulting in a more pronounced inhibition of bacterial growth. Furthermore, control laser irradiation did not influence the growth of *Porphyromonas gingivalis*, likely due to the negligible temperature change induced as shown in Figure 5b. Meanwhile, the results in *P. gingivalis* showed that our designed nanoplatform exerted significant anti-planktonic bacterial activity.

Further, biofilms are recognized for their ability to impede antibiotic penetration due to their distinctive structural and biological characteristics. To investigate further the anti-biofilm efficacy of the engineered nanoplatform against periodontal pathogens, biofilms were established by inoculating *P.g* onto saliva-coated HA discs. This setup was used to simulate the

https://doi.org/10.2147/IJN.S533622

in vivo therapeutic process for plaque removal in periodontal tissues. The *P.g* biofilms on HA discs were stained by crystal violet after various treatments (Figure 5f). The anti-biofilm activity was evaluated by disrupting the biofilm on HA discs into planktonic bacteria through ultrasonic dispersion, followed by culturing on brain heart infusion (BHI) agar medium. The CFUs from the group treated with PAg derived from *P.g* exhibited significantly enhanced anti-biofilm effects under NIR laser irradiation compared to those without NIR laser exposure (Figure 5g and h). This enhancement can be attributed to the accelerated drug release facilitated by thermotherapy and the nanoplatforms designed to penetrate the biofilm. Correspondingly, CFU quantification revealed a reduction in colony numbers to approximately 10^3 in the NIR laser-treated PAg group. These findings suggest that some bacteria within the biofilm on hydroxyapatite (HA) disks may be split away off due to the heat produced by the photothermal effect.[61] Concurrently, temperature changes were monitored during the photothermal therapy (PTT) process (Figure 5i), demonstrating an increase in photothermal conversion temperature attributable to PAg following 10 minutes of NIR laser irradiation. Notably, the maximum temperature of the HA disk was approximately 50°C, which is below the effective sterilization temperature of 60°C, thereby satisfying the criteria for low-temperature PTT.

To further investigate the potential mechanisms underlying the moderate anti-biofilm activity, we examined biofilms on hydroxyapatite (HA) discs stained with live/dead bacterial markers using confocal laser scanning microscopy (CLSM). The findings revealed a significant presence of dead bacteria, indicated by red fluorescence, within the biofilm of the laser-treated group (Figure 5j). Additionally, the results demonstrated that nanoparticles more readily penetrated or remained within the biofilm due to the obstructive nature of the biofilm matrix. The biofilm environment, composed of extracellular polymers, impedes antibiotics from reaching persistent bacterial components such as extracellular DNA, polysaccharides, and proteins. The proposed anti-biofilm mechanism underlying the observed synergistic treatment can be attributed to the elevated temperature induced by NIR laser irradiation, which disrupts bacterial adhesion to the biofilm surface and facilitates the penetration of nanoparticles into the biofilm. This process is further enhanced by the heat-assisted rapid release of silver ions from the synthesized PAg nanoparticles within the biofilm matrix. Existing literature corroborates the enhanced capability of nanoparticles to interact with biofilms and traverse extracellular polymeric substances more effectively.[62] Notably, CLSM images reveal that the PAg group exhibited a higher density of biofilm pores compared to the control group. It is essential to acknowledge that the combined mechanism warrants further investigation in subsequent studies. Despite being in the preliminary stages of exploration, our findings suggest that the fabricated nanoparticles, under NIR laser irradiation, may effectively penetrate the biofilm, potentially accounting for the observed synergistic treatment.

In vivo Therapy

Inspired by the significant in vitro antibacterial and ROS-scavenging results, we built rat model to investigate the in vivo therapeutic effect of the designed nanocomposites. Rats' periodontitis model was constructed through ligaturing the molar and injecting *P.g* to induce the infected damage of gingiva for 2~3 weeks (Figure 6a). Then, the ligature wires were dismantled and the rats were treated by injecting PAg aqueous solution into periodontal pocket and laser irradiation for about a week. At the above in vitro photothermal imaging with coincubation *Pg*, PAg revealed the excellent photothermal effect and control group remained the low temperature at the laser irradiation. To observe the temperature change of gingiva tissue after irradiating with 808-nm laser, infrared thermal imager was used to detected the temperature as displayed in Figure 6b. Comparing with the control group (directly laser irradiation after injecting PBS), the local gingiva temperature has risen by about 5 °C due to the biological tissue absorption of light.[63] As for PAg group, the temperature rose to about 52 °C, low to the demanded temperature of conventional antibacterial PTT, accord with our designed requirements. It is noted that laser spot focused on scope of infectious gingiva tissue, not affected the surrounding normal tissue, suggesting the spatiotemporal controllability and short treatment time of PTT. Besides, the temperature-rise ratio in rats' oral cavity was more rapid than that in vitro assessment (Figure 3a), may due to the high body temperature comparing with the room temperature, indicating that the temperature-rise time in vivo was lower than that in vitro.

Furthermore, to judge the biocompatibility and preliminary estimate the therapeutic effect, all groups' rat body weight varied at the rational change range (Figure S8) with injecting PAg aqueous solution every day at the process of treatment. Uniting the results of organs' H&E staining suggesting the excellent biocompatibility of PAg NPs, accorded with the

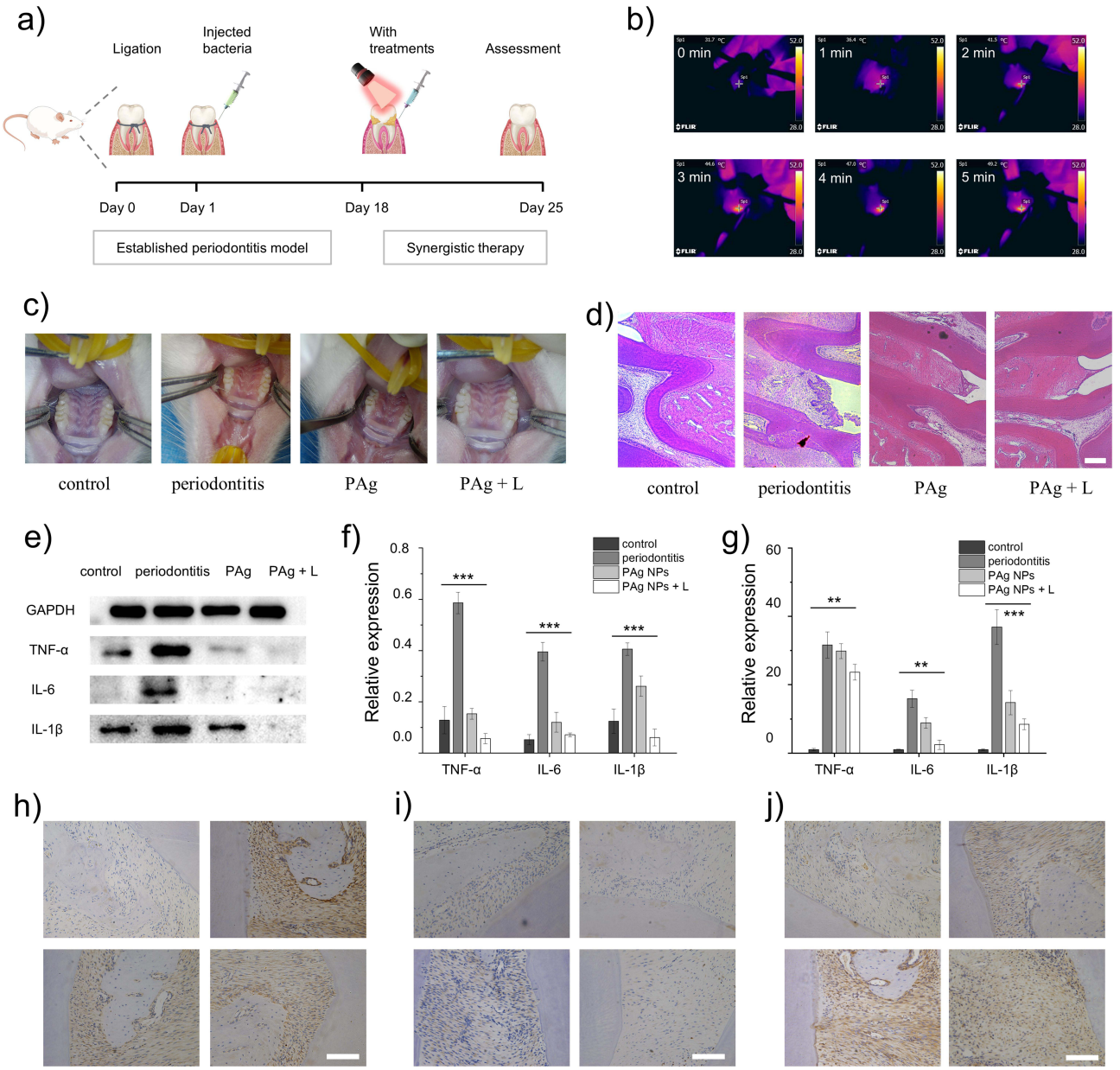

Figure 6 In vivo treatments for rat periodontitis. (**a**) Schematic diagram of the establishment of the rat periodontitis model through the ligature wire method and the process of treatments with NIR laser irradiation. (**b**) The thermal images of gingiva tissue under the irradiation of NIR laser at 1.5 W cm^{-1} for 5 min. (**c**) The oral photos of rats show the recovery of inflammation after the treatments. (**d**) HE staining of gingiva tissue at control, periodontitis, PAg and PAg + L groups. (scale bar = 250 μm). (**e**) WB, (**f**) quantified protein expression, and (**g**) PCR of TNF-α, IL-6 and IL-1β after treatments. IHC images of (**h**) TNF-α, (**i**) IL-1β, (**j**) IL-6. (scale bar = 250 μm). **P < 0.01, ***P < 0.001.

results of hemolysis test. After treatments, rat's gingiva was taken photo to intuitively observe the recovery of periodontitis (Figure 6c). The periodontitis group (rinse with PBS) still remained redness, swelling, and slight bleeding at gingiva. It is gratifying that no obvious inflammatory symptom was observed in the gingiva of PAg and PAg + L. In addition, subgingival plaque was collected through inserting the sterilized paper tip directly into the periodontal pocket, and then coated onto a medium plate and grows into a single colony. Basically, no colonies grew up in the treatment group, indicating the excellent antibacterial effect under the synergistic therapy. Moreover, the rats were sacrificed and gingival tissue was collected for H&E staining for estimating the histological recovery. As shown in Figure 6d, inflammatory cells were infiltrated at the periodontitis group, and there were almost no inflammatory cells in the

https://doi.org/10.2147/IJN.S533622

treatment group, more suggesting that the designed based-PDA nanocomposites presented anti-inflammatory capability on account of ROS-scavenging property.

To further investigate the recovery of periodontitis from the biomolecular level, the proinflammatory factors (TNF-α, IL-1β, IL-6) were evaluated by WB, QPCR, and IHC, where TNF-α has a synergistic effect with IL-1β as key promoters of the inflammatory response in periodontitis, and IL-6 is an essential regulatory factor in the acute phase of periodontitis.[52] The protein expression was obviously downregulated after treatments (Figure 6e and f), especially for the PAg + L group, indicating excellent recovery of periodontitis. At periodontitis, the relative expression of TNF-α was about 0.6, that of IL-1β was about 0.4, that of IL-6 was about 0.4. It is noteworthy that the recovery of laser irradiation group was better, indicating that the synergistic therapy from mild PTT and silver nanoparticles is more superior. Further, the expressions of TNF-α, IL-1β, and IL-6 mRNA at transcriptional level were detected as shown in Figure 6g, indicate that the reduced expression of TNF-α, IL-1β, and IL-6 post-treatment not only reflects the resolution of inflammation but also suggests the effectiveness of the treatment measures. Besides, according to the immunohistochemical image coloration (Figure 6h–j), TNF-α, IL-1β, and IL-6 in the inflammatory group showed strong brown-yellow, indicating high-quantity expression in inflammation. High TNF-α expression drives inflammatory cells to gather in gum tissue, triggering an inflammatory cascade. The strong IL-1β color shows its active role in amplifying inflammation and collaborating with TNF-α to damage periodontal tissue.[64] The significant IL-6 coloration means it has pro-inflammatory and immunomodulatory functions in acute-phase inflammation, worsening tissue damage. In the treatment group, coloration was greatly reduced. This means post-treatment, TNF-α, IL-1β, and IL-6 expressions are significantly lower. The key drivers of inflammation are inhibited, reducing inflammatory cell chemotaxis and activation, effectively controlling inflammation, showing the treatment successfully alleviates gum tissue inflammation.

In the rat periodontitis model, the subgingival biofilm was constructed by *Pg* bacteria (as main pathogenic bacteria of periodontitis) colonization to induce periodontal inflammation. Over the course of therapy, the complex structure of biofilms made them particularly challenging to completely eradicate by PAg nanoplatforms. Hyperthermia produced by PAs under laser light (PAg + L) could disrupt the biofilm, facilitating the penetration of Ag^+ and the synergistic therapy. In addition, laser irradiation could boost the catalytic efficiency of the nanozymes by speeding up electron migration,[65] aiding in the removal of ROS to enhance anti-inflammatory capacity by inhibiting inflammatory factors. The anti-inflammatory property of PDA plays a key role at the treatment,[66] according with the results of ROS scavenging. Simultaneously, the protection of PDA as antioxidant agent may reduce the damage for the normal tissue from silver. Hence, the encouraging findings implied that the designed PAg nanoplatform could present favorable prospects for subsequent clinical treatment of periodontitis.

Biocompatibility

Biocompatibility pertains to the characteristics of a material that elicits no adverse reactions, is non-toxic, and can sustain tissue functionality in interaction with a biological organism. This assessment is particularly crucial for nanobiomaterials, as inappropriate material design or application may result in inflammatory responses, immune rejection, or toxic reactions. Consequently, the biocompatibility properties of PDA at the cellular level, including in vitro cytotoxicity, in vivo hemolysis tests, and in vivo acute toxicity, require further investigation. In the context of local periodontal therapy, the biocompatibility of PDA nanocarriers was assessed using periodontal membrane fibroblasts (HPLCs) and macrophages (Raw264.7) as model cell lines. The impact of PDA was further validated through 24-hour cell viability assays, as evidenced by live/dead staining (Figure 7a). The CCK8 assay results indicated a slight reduction in cell density relative to the control group; however, the presence of very few dead cells, as evidenced by red fluorescence with EB staining, suggests that the synthesized nanocarriers exhibit minimal cytotoxicity. Furthermore, following 24, 48, and 72 hours of co-incubation, the cell survival rate declined as the concentration of PDA increased to 800 μg mL^{-1} (Figure 7b). Despite this, the CCK8 results demonstrated that the nanocarriers maintained a biocompatibility level exceeding 75%. These findings indicate that the PDA exhibits substantial biocompatibility. Additionally, the hemolysis rate of PDA remained below 5% across the concentration range of 50 to 800 μg mL^{-1}, indicating favorable blood compatibility. Histological examination through H&E staining (Figure 7d) revealed no significant tissue damage in major

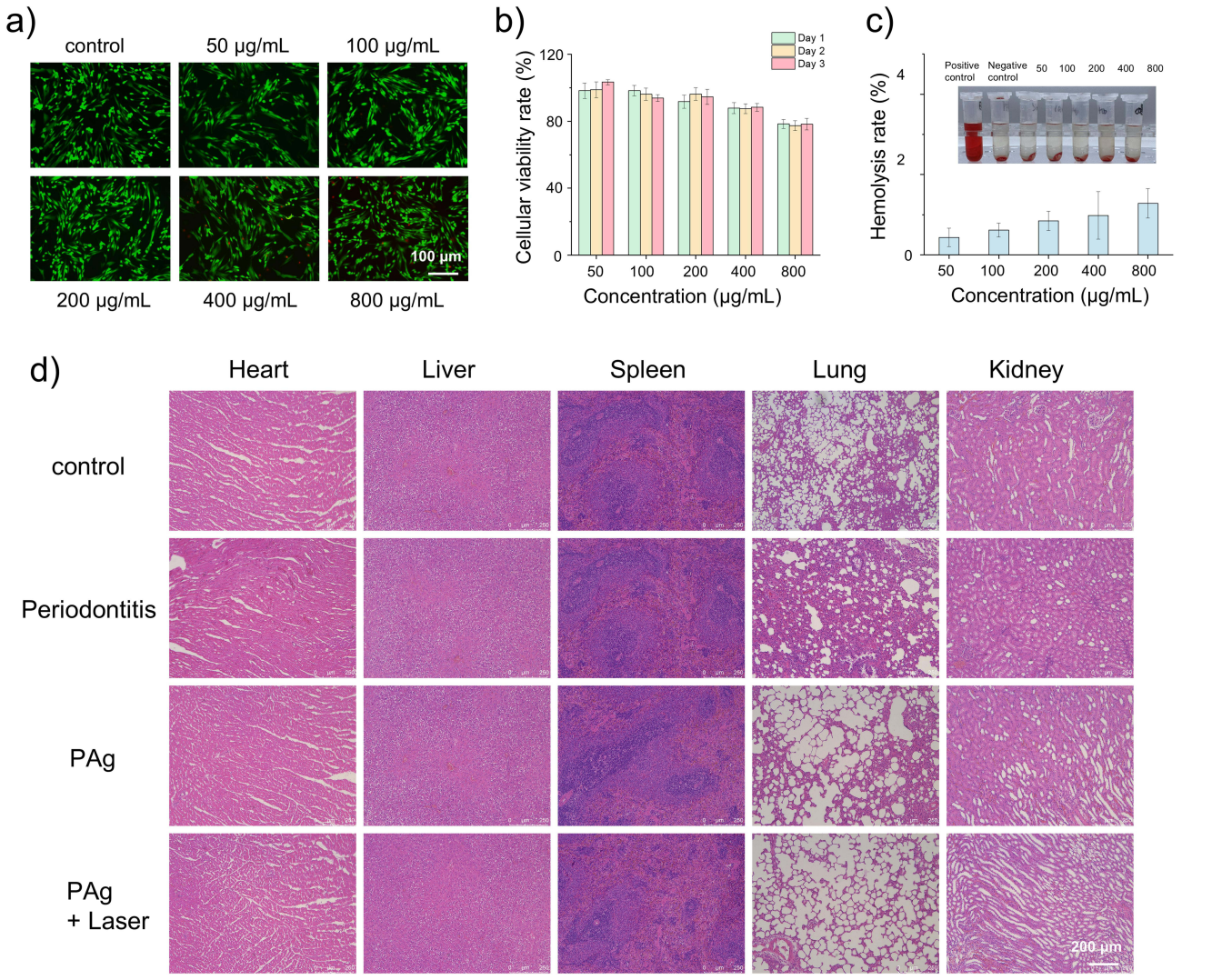

Figure 7 Biocompatibility of the designed nanocomposites. (**a**) Hemolysis rate of PDA at various concentration. (**b**) Cellular viability rate of HPLCs by CCK8 method. (**c**) AO/EB double staining kit. (**d**) H&E results of major organs (heart, liver, spleen, lung, kidney) of rats.

organs, including the heart, liver, lungs, spleen, and kidneys, further corroborating the excellent biocompatibility of the nanocarriers.

While we successfully established a multifunctional nanozyme-based therapeutic platform, several limitations require further exploration. Although PAg demonstrated stability in simulated physiological fluids, its long-term performance evolution in complex oral microenvironments—characterized by dynamic pH fluctuations, protease enrichment, and biofilm matrix penetration—remains uncharacterized, particularly regarding the interaction between in situ-synthesized silver nanoparticles and sulfide-rich periodontal pockets. In addition, while we focused on pro-inflammatory factor regulation, molecular-level validation of key signaling pathways critical for periodontal tissue regeneration is lacking. Moreover, the local retention time of nanomaterials under salivary flow and their ecological impact on the oral microbiome remain unassessed, potentially compromising clinical translation reliability. Hence, future research should prioritize: (1) developing intelligent responsive nanosystems integrating pH/ROS dual-sensitive motifs for precision drug release, coupled with microfluidic chip-simulated oral hydrodynamic conditions to enhance material retention; and (2) exploring synergistic effects between nanomaterials and periodontal ligament stem cell differentiation through epigenetic regulation to elucidate osteogenic mechanisms. These advancements will bridge the gap between foundational research and clinical translation, enabling transformative progress in precision oral therapeutics.

https://doi.org/10.2147/IJN.S533622

Conclusions

In summary, we have successfully developed a multifunctional nanozyme-based local platform employing dopamine self-polymerization to synthesize PDA nanozymes as a core for the removal of excess ROS and RNS from periodontal tissue injuries. Comprehensive characterization revealed the nanoplatforms' favorable morphological properties, core-satellite structure, uniform dispersion, and significant stability in PBS, artificial saliva, and FBS. Additionally, they exhibited good photothermal conversion efficiency and stability under near-infrared laser irradiation. These multifunctional nanoplatforms demonstrated significant ROS scavenging capabilities, including H_2O_2,·OH, and O_2, as evidenced by the reducibility of catechol in PDA, enzyme activity assays, and cellular ROS assessments. Beyond enhancing ROS clearance in inflamed tissues, PDA also leverages its reducibility to facilitate the in situ synthesis of nanosilver on its surface. Furthermore, the nanocomposite we developed demonstrates the capability to not only eliminate cellular ROS in cells such as RAW264.7 and HPDLCs, but also to enhance the antibacterial membrane effect through mild PTT, attributed to the superior photothermal conversion properties of PDA. Additionally, thermal therapy under near-infrared laser irradiation facilitates the release of nanodispersions and accelerates the penetration of nanocomposites into biofilms, thereby improving biofilm removal efficacy. Moreover, our localized drug delivery system employs antibacterial PTT to enhance therapeutic outcomes while mitigating antibiotic overuse. In vivo studies corroborate these advantages by evaluating the therapeutic effects of nanocomposites under near-infrared laser irradiation and assessing the anti-inflammatory impacts on cytokines such as IL-6, IL-1β, and TNF-α. Collectively, our results indicate that this novel nanoparticle-based hybrid platform, utilizing combination therapy, holds significant potential for the effective treatment of periodontitis and the reduction of excess ROS, thereby alleviating inflammation.

Funding

We sincerely acknowledge the financial support from the Technological Plan of Health Commission of Jiangxi Province of China (202410037), the Technological Plan of Traditional Chinese Medicine Administration of Jiangxi Province of China (2024B0483), the National Natural Science Foundation of China (82460185), the Natural Science Foundation Projects of Jiangxi Province (20232ACB206028, 20252BAC240569).

Disclosure

The authors report no conflicts of interest in this work.

References

1. Slots J. Periodontitis: facts, fallacies and the future. *Periodontology 2000*. 2017;75(1):7–23. doi:10.1111/prd.12221
2. Kim T-H, Heo S-Y, Chandika P, et al. A literature review of bioactive substances for the treatment of periodontitis: in vitro, in vivo and clinical studies. *Heliyon*. 2024;10(2):e24216. doi:10.1016/j.heliyon.2024.e24216
3. Guo J, Wang P, Li Y, et al. Advances in hybridized nanoarchitectures for improved oro-dental health. *J Nanobiotechnol*. 2024;22(1). doi:10.1186/s12951-024-02680-5
4. Sczepanik FSC, Grossi ML, Casati M, et al. Periodontitis is an inflammatory disease of oxidative stress: we should treat it that way. *Periodontology 2000*. 2020;84(1):45–68. doi:10.1111/prd.12342
5. Sui L, Wang J, Xiao Z, et al. ROS-scavenging nanomaterials to treat periodontitis. *Front Chem*. 2020;8:595530. doi:10.3389/fchem.2020.595530
6. Liu J, Han X, Zhang T, et al. Reactive oxygen species (ROS) scavenging biomaterials for anti-inflammatory diseases: from mechanism to therapy. *J Hematol Oncol*. 2023;16(1):116. doi:10.1186/s13045-023-01512-7
7. Wang P, Wang L, Zhan Y, et al. Versatile hybrid nanoplatforms for treating periodontitis with chemical/photothermal therapy and reactive oxygen species scavenging. *Chem Eng J*. 2023;463:142293. doi:10.1016/j.cej.2023.142293
8. Han M, Tang K, Chen Z. Preparation of NIR responsive resveratrol@Au nanocages using for regulating oxidative stress microenvironment of periodontitis. *Chem Eng J*. 2025;504:158774. doi:10.1016/j.cej.2024.158774
9. Lam W, Yao Y, Tang C, et al. Bifunctional mesoporous HMUiO-66-NH2 nanoparticles for bone remodeling and ROS scavenging in periodontitis therapy. *Biomaterials*. 2025;314:122872. doi:10.1016/j.biomaterials.2024.122872
10. Nasser Atia GA, Mohamed SZ, Taymour N, et al. Carbon dots as promising carbon nanomaterials for diagnostics, therapeutics, and regenerative orofacial applications. *J Drug Delivery Sci Technol*. 2025. doi:10.1016/j.jddst.2025.106808
11. Atia GA, Abdal Dayem A, Taher ES, et al. Urine-derived stem cells: a sustainable resource for advancing personalized medicine and dental regeneration. *Front Bioeng Biotechnol*. 2025;13. doi:10.3389/fbioe.2025.1571066
12. Li Y, Muhammad F, Chen X, et al. Smart multifunctional Cu2O@RuO2 nanozyme for angiogenesis and osteogenesis in periodontitis. *Nano Today*. 2025;61:102624. doi:10.1016/j.nantod.2024.102624
13. Li Z, Fan X, Liu Y, et al. Engineering mild-photothermal responsive and NO donor prussian blue nanozymes using mild synthesis for inflammation regulation and bacterial eradication in periodontal disease. *Adv Mater*. 2024. doi:10.1002/adma.202409840

14. Wan S, Liu W, Wu Q, et al. Nanobiohybrid extracellular vesicle nanoreactor with improving metabolical activity for biocatalytic therapy. *ACS nano*. 2024;18(47):32899–32909. doi:10.1021/acsnano.4c12458
15. Zhang L, Wang Y, Wang C, et al. Light-activable on-demand release of nano-antibiotic platforms for precise synergy of thermochemotherapy on periodontitis. *ACS Appl Mater Interfaces*. 2020;12(3):3354–3362. doi:10.1021/acsami.9b17335
16. Huang Y, Liu Y, Pandey NK, et al. Iron oxide nanozymes stabilize stannous fluoride for targeted biofilm killing and synergistic oral disease prevention. *Nat Commun*. 2023;14(1). doi:10.1038/s41467-023-41687-8
17. He Y, Tang Y, Zeng B, et al. Black phosphorus quantum dot-modified ADSCs as a novel therapeutic for periodontitis bone loss coupling of osteogenesis and osteoimmunomodulation. *Mater Today Bio*. 2024;27:101122. doi:10.1016/j.mtbio.2024.101122
18. Liu W, Shi E, Wu H, et al. Spatially axial boron coordinated single-atom nanozymes with boosted multi-enzymatic performances for periodontitis treatment. *Adv Funct Mater*. 2024;34(39). doi:10.1002/adfm.202403386
19. Yu Y, Zhao S, Gu D, et al. Cerium oxide nanozyme attenuates periodontal bone destruction by inhibiting the ROS-NFkappaB pathway. *Nanoscale*. 2022;14(7):2628–2637. doi:10.1039/d1nr06043k
20. Özdoğan AI, Ilarslan YD, Kösemehmetoğlu K, et al. In vivo evaluation of chitosan based local delivery systems for atorvastatin in treatment of periodontitis. *Int J Pharm*. 2018;550(1–2):470–476. doi:10.1016/j.ijpharm.2018.08.058
21. Huang M, Ke C, Yang L, et al. Self-propelled MnO2 -based colloidal motors for active treatment of periodontal inflammation. *Chem – Asian J*. 2025;20(11). doi:10.1002/asia.202500157
22. Fu Y, Yang L, Zhang J, et al. Polydopamine antibacterial materials. *Mater Horizons*. 2021;8(6):1618–1633. doi:10.1039/d0mh01985b
23. Wang P, Chen R, Jia Y, et al. Cu-chelated polydopamine nanozymes with laccase-like activity for photothermal catalytic degradation of dyes. *J Colloid Interface Sci*. 2024;669:712–722. doi:10.1016/j.jcis.2024.04.124
24. Shi F, Chen J, Yan L, Tu J. GSH-depleting and H2O2 self-supplying calcium peroxide-based nanoplatforms for efficient bacterial eradication via photothermal-enhanced chemodynamic therapy. *ACS Appl Mater Interfaces*. 2024;16(50):69055–69070. doi:10.1021/acsami.4c17388
25. Xu H, Zhang Y, Zhang H, et al. Smart polydopamine-based nanoplatforms for biomedical applications: state-of-art and further perspectives. *Coord Chem Rev*. 2023;488:215153. doi:10.1016/j.ccr.2023.215153
26. Wang K, Mao W, Song X, et al. Composition-reinforced polydopamine nanoenzyme for improved impairment of prostatitis-damaged sexual behavior and enhanced anti-prostate cancer. *Adv Funct Mater*. 2024;34(19). doi:10.1002/adfm.202313528
27. Bao X, Zhao J, Sun J, et al. Polydopamine nanoparticles as efficient scavengers for reactive oxygen species in periodontal disease. *ACS nano*. 2018;12(9):8882–8892. doi:10.1021/acsnano.8b04022
28. Zeng J, Wang Y, Sun Z, et al. A novel biocompatible PDA/IR820/DAP coating for antibiotic/photodynamic/photothermal triple therapy to inhibit and eliminate Staphylococcus aureus biofilm. *Chem Eng J*. 2020;394:125017. doi:10.1016/j.cej.2020.125017
29. Yu X, Zhao J, Fan D. A dissolving microneedle patch for Antibiotic/Enzymolysis/Photothermal triple therapy against bacteria and their biofilms. *Chem Eng J*. 2022;437:135475. doi:10.1016/j.cej.2022.135475
30. Sheng L, Feng Y, Wu S, et al. Biodegradable copper vanadate-based hydrogel with photocatalytic/photothermal therapy for infected diabetic wound healing. *Mater Des*. 2024;246:113358. doi:10.1016/j.matdes.2024.113358
31. Yang Y, Cai Q, Wang L, et al. Oxygen-deficient Bi2MoO6@sRuO2@HA heterojunction for photocatalytic treatment of drug-resistant bacterial infections. *Chem Eng J*. 2024;502:157828. doi:10.1016/j.cej.2024.157828
32. Xu X, Chen X, Wang H, et al. Balancing the toxicity, photothermal effect, and promotion of osteogenesis: photothermal scaffolds for malignant bone tumor therapy. *Mater Today Adv*. 2022;13:100209. doi:10.1016/j.mtadv.2022.100209
33. Zhang X, Tan B, Wu Y, et al. A review on hydrogels with photothermal effect in wound healing and bone tissue engineering. *Polymers*. 2021;13 (13). doi:10.3390/polym13132100
34. Chaloupka K, Malam Y, Seifalian AM. Nanosilver as a new generation of nanoproduct in biomedical applications. *Trends Biochem Sci*. 2010;28 (11):580–588.
35. Streich C, Stein F, Jakobi J, et al. The origin of the intracellular silver in bacteria: a comprehensive study using targeting gold–silver alloy nanoparticles. *Adv Healthc Mater*. 2023;12(30). doi:10.1002/adhm.202302084
36. Li X, Shang H, Xiong Y, et al. Silver/jellyfish-like mesoporous polydopamine nanomotor with concentration-dependent synergistic antibacterial activity. *Chem Eng J*. 2025;505. doi:10.1016/j.cej.2025.159367
37. Zhang Y, Sun P, Zhang L, et al. Silver-infused porphyrinic metal–organic framework: surface-adaptive, on-demand nanoplatform for synergistic bacteria killing and wound disinfection. *Adv Funct Mater*. 2019;29(11). doi:10.1002/adfm.201808594
38. He L, Xing S, Zhang W, et al. Multifunctional dynamic chitosan-guar gum nanocomposite hydrogels in infection and diabetic wound healing. *Carbohydr Polym*. 2025;354:123316. doi:10.1016/j.carbpol.2025.123316
39. Li W, Tang Y, Liu B, et al. Research progress of gold, silver, and copper nanoclusters in bacterial infection diagnosis and treatment. *Chem Eng J*. 2025;506. doi:10.1016/j.cej.2025.159977
40. Zhu M, Wang P, Chen B, et al. Active-oxygenating hollow Prussian blue nanosystems loaded with biomacromolecules for photodynamic/ photothermal therapy of cancer and alleviating hypoxic tumors. *Mater Des*. 2024;237:112618. doi:10.1016/j.matdes.2023.112618
41. Li Y, Wang P, Liu Y, et al. Fe3O4-based nanospheres with high photothermal conversion efficiency for dual-effect and mild biofilm eradication against periodontitis. *ACS Appl Mater Interfaces*. 2025. doi:10.1021/acsami.4c17966
42. Liu YC, Lin YK, Lin YT, et al. Injectable, antioxidative, and tissue-adhesive nanocomposite hydrogel as a potential treatment for inner retina injuries. *Adv Sci*. 2024;11(11). doi:10.1002/advs.202308635
43. Wang L, Song K, Jiang C, et al. Metal-coordinated polydopamine structures for tumor imaging and therapy. *Adv Healthc Mater*. 2024;13(28). doi:10.1002/adhm.202401451
44. Yang Y, Murray J, Haverstick J, et al. Silver nanotriangle array based LSPR sensor for rapid coronavirus detection. *Sensors and Actuat B Chem*. 2022;359:131604. doi:10.1016/j.snb.2022.131604
45. Zhao Y, Zhao T, Cao Y, et al. Temperature-sensitive lipid-coated carbon nanotubes for synergistic photothermal therapy and gene therapy. *ACS nano*. 2021;15(4):6517–6529. doi:10.1021/acsnano.0c08790
46. Lv Z, He S, Wang Y, Zhu X. Noble metal nanomaterials for NIR-triggered photothermal therapy in cancer. *Adv Healthc Mater*. 2021;10(6). doi:10.1002/adhm.202001806

47. Chen Y, Ran Y, Rao Z, et al. Self-assembled chemo/photothermal nanoplatform for enhanced cancer therapy: sensitizing photothermal ablation and reprogramming inflammatory microenvironment. *ACS Mater Lett*. 2024;6(9):3915–3924. doi:10.1021/acsmaterialslett.4c01066
48. Zhao P, Zhang Y, Chen X, et al. Versatile hydrogel dressing with skin adaptiveness and mild photothermal antibacterial activity for methicillin-resistant staphylococcus aureus-infected dynamic wound healing. *Adv Sci*. 2023;10(11):2206585. doi:10.1002/advs.202206585
49. Yaqoob MD, Xu L, Li C, et al. Targeting mitochondria for cancer photodynamic therapy. *Photodiagnosis Photodyn Ther*. 2022;38:102830. doi:10.1016/j.pdpdt.2022.102830
50. Nie M, Zhang P, Pathak JL, et al. Photodynamic therapy in periodontitis: a narrative review. *Photodermatol Photoimmunol Photomed*. 2024;40(1). doi:10.1111/phpp.12946
51. Zhao M, Yang J, Liang J, et al. Emerging nanozyme therapy incorporated into dental materials for diverse oral pathologies. *Dent Mater*. 2024;40 (11):1710–1728. doi:10.1016/j.dental.2024.07.025
52. Zhao W, Zhang Y, Chen J, Hu D. Revolutionizing oral care: reactive oxygen species (ROS)-Regulating biomaterials for combating infection and inflammation. *Redox Biol*. 2025;79. doi:10.1016/j.redox.2024.103451
53. Han J, Wang J, Shi H, et al. Ultra-small polydopamine nanomedicine-enabled antioxidation against senescence. *Mater Today Bio*. 2023;19:100544. doi:10.1016/j.mtbio.2023.100544
54. Shen X, Liu W, Gao X, et al. Mechanisms of oxidase and superoxide dismutation-like activities of gold, silver, platinum, and palladium, and their alloys: a general way to the activation of molecular oxygen. *J Am Chem Soc*. 2015;137(50):15882–15891. doi:10.1021/jacs.5b10346
55. Guo J, Yang H, Liu Y, et al. Atomically precise silver clusterzymes protect mice from radiation damages. *J Nanobiotechnol*. 2021;19(1). doi:10.1186/s12951-021-01054-5
56. Lei Y, Wang K, Deng L, et al. Redox regulation of inflammation: old elements, a new story. *Med Res Rev*. 2014;35(2):306–340. doi:10.1002/med.21330
57. Zhao Y, Liu H, Xi X, et al. TRIM16 protects human periodontal ligament stem cells from oxidative stress-induced damage via activation of PICOT. *Exp Cell Res*. 2020;397(1):112336. doi:10.1016/j.yexcr.2020.112336
58. Bhol NK, Bhanjadeo MM, Singh AK, et al. The interplay between cytokines, inflammation, and antioxidants: mechanistic insights and therapeutic potentials of various antioxidants and anti-cytokine compounds. *Biomed Pharmacother*. 2024;178:117177. doi:10.1016/j.biopha.2024.117177
59. Jomova K, Alomar SY, Alwasel SH, et al. Several lines of antioxidant defense against oxidative stress: antioxidant enzymes, nanomaterials with multiple enzyme-mimicking activities, and low-molecular-weight antioxidants. *Arch Toxicol*. 2024;98(5):1323–1367. doi:10.1007/s00204-024-03696-4
60. Chinmaya Mutalik GO, Krisnawati DI, Jazidie A, et al. Copper sulfide with morphology-dependent photodynamic and photothermal antibacterial activities. *J Colloid Interface Sci*. 2022;607:1825–1835. doi:10.1016/j.jcis.2021.10.019
61. Yuan Z, Lin C, He Y, et al. Near-infrared light-triggered nitric-oxide-enhanced photodynamic therapy and low-temperature photothermal therapy for biofilm elimination. *ACS nano*. 2020;14(3):3546–3562. doi:10.1021/acsnano.9b09871
62. Fulaz S, Vitale S, Quinn L, Casey E. Nanoparticle–biofilm interactions: the role of the EPS matrix. *Trends Microbiol*. 2019;27(11):915–926. doi:10.1016/j.tim.2019.07.004
63. Bashkatov AN, Genina EA, Kochubey VI, Tuchin VV. Optical properties of human skin, subcutaneous and mucous tissues in the wavelength range from 400 to 2000 nm. *J Phy D App Phy*. 2005;38(15):2543–2555. doi:10.1088/0022-3727/38/15/004
64. Wu Q, Zhang W, Lu Y, et al. Association between periodontitis and inflammatory comorbidities: the common role of innate immune cells, underlying mechanisms and therapeutic targets. *Int Immunopharmacol*. 2024;128:111558. doi:10.1016/j.intimp.2024.111558
65. V. g S, Mangalsana H, Vernekar A. Breaking barriers in photothermal tumor therapy: a cascade of strain-engineered nanozyme in action. *ChemMedChem*. 2024;19(22). doi:10.1002/cmdc.202400443
66. Wang W, Zheng J, Zhou H, et al. Polydopamine-based nanocomposite as a biomimetic antioxidant with a variety of enzymatic activities for Parkinson's disease. *ACS Appl Mater Interfaces*. 2022. doi:10.1021/acsami.2c06981